Chemical Science

ROYAL SOCIETY OF CHEMISTRY

EDGE ARTICLE

View Article Online
View Journal

Cite this: DOI: 10.1039/d6sc02037b

All publication charges for this article have been paid for by the Royal Society of Chemistry

Charge-regulated hepatic γ-glutamyltranspeptidase fluorescent probe: *in vivo* staging of *Schistosoma* infection

Xiaoxi Ma,[a] Eryang Xie,[a] Qiang Li,[c] Chuyang Sun,[a] Yongkang Yao,[a] Chenxu Yan, *[a] Qianfu Luo,*[a] Zhiqian Guo *[ab] and Wei-Hong Zhu [a]

Schistosomiasis remains a formidable global health threat, yet with the limited sensitivity and critical inability of real-time *in vivo* monitoring using current diagnostic modalities such as microscopy and ultrasonography, there are significant hurdles to overcome before precise infection staging can be performed. To address this diagnostic bottleneck, we developed a *de novo* strategic charge-regulation approach with a dual-channel near-infrared fluorescent probe that binds to hepatic γ-glutamyltranspeptidase (GGT), a key biomarker for schistosomiasis-induced liver pathological evolution. By engineering quinoline scaffolding from zwitterionic, single-positive charge, to double-positive charge, the optimized probe QMC-N-GGT achieved superior precise targeting of infected liver tissues in an anionic microenvironment. Impressively, its breakthrough dual-channel signals enable tracking of when, where, and how the probe targets the liver and illuminates endogenous GGT *in situ*. This probe exhibits a remarkable stage-dependent fluorescent response to GGT, enabling accurate distinction of slight, moderate, and severe infection stages with an ultra-high signal-to-noise ratio. QMC-N-GGT thus represents an unprecedented diagnostic tool, bridging the gap between conventional infection screening and advanced pathological staging for non-invasive, real-time schistosomiasis monitoring.

Received 11th March 2026
Accepted 16th April 2026

DOI: 10.1039/d6sc02037b

rsc.li/chemical-science

Introduction

Schistosomiasis, caused by trematode flukes of the genus *Schistosoma*, is the second most prevalent parasitic disease worldwide.[1–4] Triggered by tissue-trapped eggs, schistosomiasis leads to severe pathologies ranging from systemic symptoms to multi-organ damage, such as severe hepatosplenism and progressive fibrosis.[5–7] Three distinct phases exist in schistosomiasis progression (acute infection, established active infection, and late chronic infection), with each stage requiring specific therapeutic interventions.[8,9] Thus, real-time staging and evolutionary identification of *Schistosoma* infection are essential for clinical management. However, a fundamental challenge is how to non-invasively assess these dynamic staging processes *in vivo*.

Current approaches harness *in vitro* detection (Fig. 1A), relying on microscopic counting of viable eggs in urine, faeces, or tissue biopsies. Because of the limited sensitivity, the presence of infecting schistosomes cannot be definitively ruled out. As for *in vivo* diagnosis, ultrasonography is generally confined to detecting pathological changes in the late stages of infection. Consequently, a tool that could identify the spatiotemporal progression across stages would be of crucial importance in the clinical management of schistosome-induced conditions.

Fluorescence-based technologies[10–14] have revolutionized the *in vivo* monitoring of biomarkers.[15–19] Especially for schistosomiasis, γ-glutamyltransferase (GGT) has emerged as a crucial enzymatic marker,[20–22] as it is markedly upregulated during schistosomiasis-induced hepatic granuloma formation and subsequent fibrosis,[2,23,24] with its catalytic activity showing a strong positive correlation with the infectious progression.[25–27] As such, developing activatable probes to track hepatic GGT activity presents an effective strategy for the real-time staging of schistosomiasis.[28–30] However, the intrinsic pathological complexity of *Schistosoma* infection, characterized by deep-tissue hepatic sequestration and dynamic evolution features, poses significant hurdles for probe design.[31–35] In this regard, we reasoned that two prerequisites are essential: one is to

[a]*Key Laboratory for Advanced Materials and Institute of Fine Chemicals, Feringa Nobel Prize Scientist Joint Research Center, Frontiers Science Center for Materiobiology and Dynamic Chemistry, School of Chemistry and Molecular Engineering, East China University of Science and Technology, Shanghai 200237, China. E-mail: chenxuyan@ecust.edu.cn; luoqf@ecust.edu.cn; guozq@ecust.edu.cn*

[b]*State Key Laboratory of Bioreactor Engineering, East China University of Science and Technology, Shanghai 200237, China*

[c]*National Key Laboratory of Intelligent Tracking and Forecasting for Infectious Diseases, National Institute of Parasitic Diseases at Chinese Center for Disease Control and Prevention, Chinese Center for Tropical Diseases Research, National Research Center for Tropical Diseases, Key Laboratory of Parasite and Vector Biology, National Health Commission, WHO Collaborating Center for Tropical Diseases, National Center for International Research on Tropical Diseases, Ministry of Science and Technology, Shanghai 20025, China*

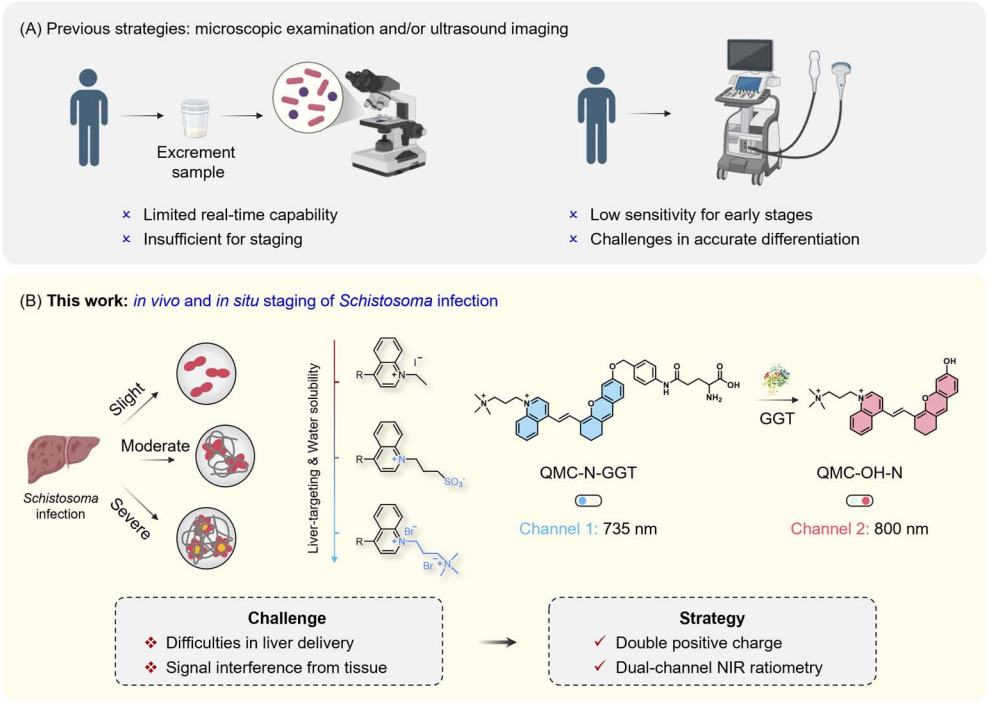

Fig. 1 Double-positive-charged NIR fluorescent probe: dual-channel mapping of liver γ-glutamyltranspeptidase for staging *Schistosoma* infection. (A) Limitations of current diagnostics for staging *Schistosoma* infection. (B) Double-positive-charged NIR probe for dual-channel mapping of hepatic γ-glutamyltransferase (GGT), enabling the intact *in vivo* staging of schistosomiasis progression.

modulate the charge properties of the molecular scaffold to optimize the pharmacokinetics for hepatotropic enrichment;[36–40] the other is to incorporate an additional emission channel to transform conventional 'turn-on' probes into dual-channel ratiometric sensors, thus enabling high-fidelity identification of GGT activity *in situ* and *in vivo*.

Herein, we present a charge-regulated dual-channel near infrared (NIR) probe strategy to address the limitations of traditional microscopic examination and ultrasonography in schistosomiasis monitoring. This strategy is centered on a quinoline scaffold, featuring precisely tailored charged centers[41–44] (from zwitterionic, single-positive charge, to double-positive charge) that optimize the pharmacokinetic behavior for hepatotropic enrichment and retention (Fig. 1B). Our optimized probe, QMC-N-GGT, integrates a dicationic core to significantly enhance the systemic circulation and liver-targeting capability *via* electrostatic attraction to the anionic microenvironment of damaged liver tissues. Crucially, its dual-channel ratiometric signaling provides real-time feedback to track when, where, and how the probe targets the liver and illuminates endogenous GGT *in situ*.

The *in vivo* imaging results provide solid evidence that QMC-N-GGT can markedly differentiate among the evolutionary stages of severity (including slight, moderate, and severe infection stages) *via* the fluorescent response kinetics and intensity. This integrated approach offers an intact molecular imaging platform for the high-fidelity *in vivo* staging of schistosomiasis, representing a potent chemical tool for multiscale assessment of infection dynamics.

Results and discussion

Double-positive-charged quinoline NIR fluorophore with hepatic targeting and retention

Given that the pathogenesis of schistosomiasis is characterized by the formation of spatially heterogeneous hepatic fibrosis, an effective imaging agent must meet two key criteria: efficient liver accumulation to target infection sites and NIR fluorescence to ensure sufficient penetration for deep liver imaging. To address these requirements, we selected quinoline as the fluorophore building block due to its inherent sensitivity to electronic modifications and tunable intramolecular charge transfer (ICT) characteristics. As established, the major components of the liver extracellular matrix (ECM) include glycoproteins and negatively charged proteoglycans, such as chondroitin sulfate, biglycan, and decorin.

In a fibrotic liver, the ECM components are similar to those in a normal liver but are quantitatively increased, leading to an increase in the overall negative charge.[45,46] As such, we reasoned that a charge-regulation approach could improve the probe's hepatic targeting and retention. With this in mind, we designed and synthesized a series of quinoline-based candidates with distinct electronic properties (Fig. 2A): QMC-OH-C (single-positive charged), QMC-OH-SO_3 (zwitterionic), and QMC-OH-N (double-positive charged). As expected, all derivatives exhibit typical NIR properties, with absorption and emission maxima centered at approximately 580 nm and 735 nm, respectively (Fig. 2B and C). Then, we examined how charge characteristics serve as a key determinant of the fluorophores' water solubility and pharmacokinetic behavior.

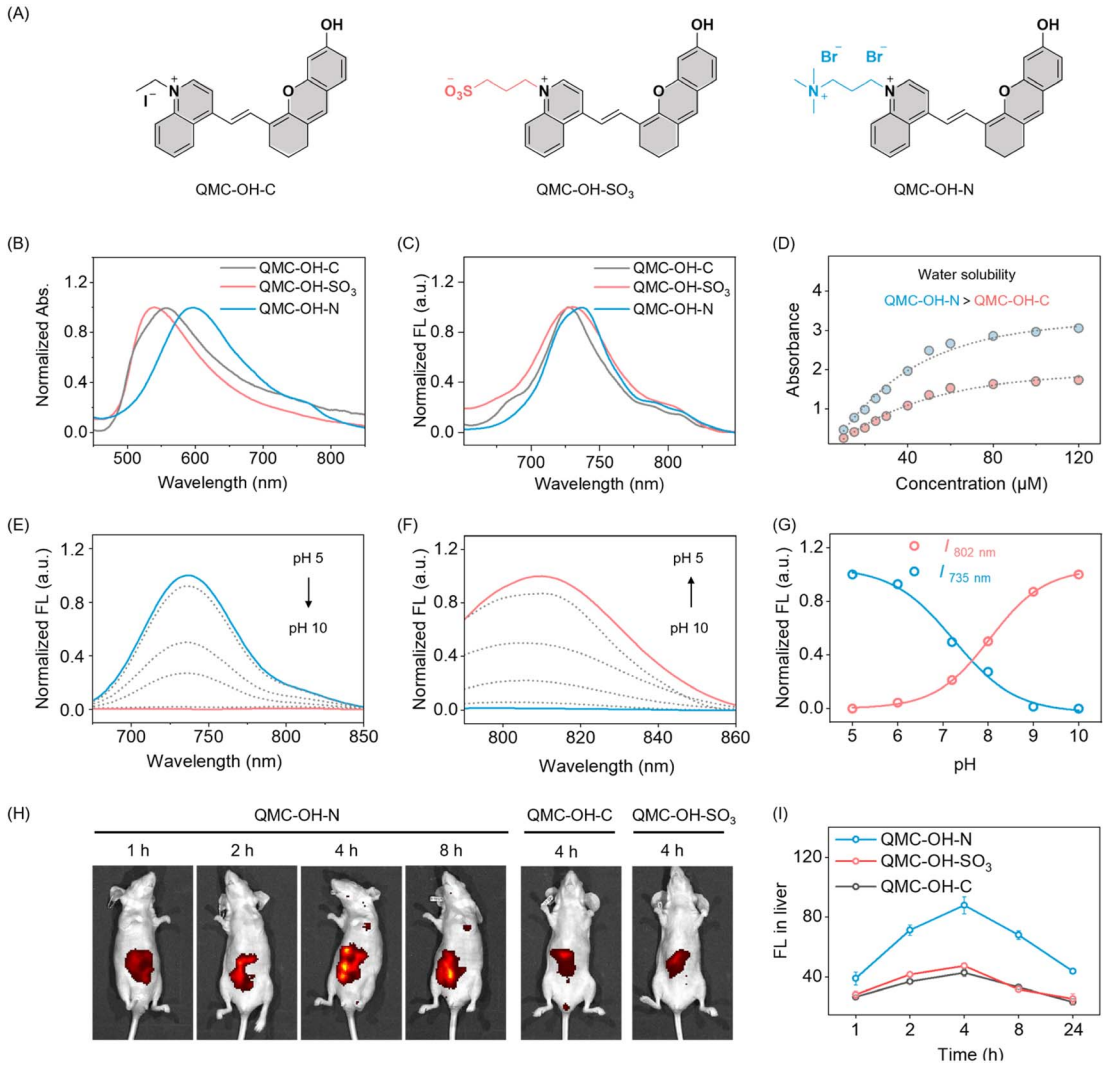

Fig. 2 Charge-modulated quinoline NIR fluorophores with good miscibility and liver targeting. (A) Chemical structures of three tailored NIR fluorescent probes: QMC-OH-C, QMC-OH-SO_3, and QMC-OH-N. (B and C) Normalized absorption (B) and fluorescence (C) spectra of the QMC dyes in aqueous solution, exhibiting characteristic NIR emission centered at approximately 735 nm (λ_{ex} = 620 nm, 10 μM). (D) Comparative water solubility evaluation. The concentration-dependent absorbance plots highlight the superior linear dynamic range and improved dispersity of the cationic QMC-OH-N compared to the anionic QMC-OH-C. (E and F) pH-dependent fluorescence response of QMC-OH-N (10 μM, pH 5.0 to 10.0, λ_{ex} = 620 nm). (G) Ratiometric pH titration curves based on the fluorescence intensity ratio. (H) Representative real-time NIR fluorescence images of healthy mice at different time intervals (1, 2, 4, and 8 h) after intravenous injection of QMC-OH-C, QMC-OH-SO_3, and QMC-OH-N. (I) Time-dependent fluorescence intensity profiles in the liver region of mice (n = 3). Data are expressed as mean ± s.d.

To assess the water solubility, we obtained the concentration-dependent absorbance spectra. As shown in Fig. 2D and S1, QMC-OH-N maintains a consistently higher absorbance than QMC-OH-C across the tested concentration range, indicating greater miscibility of QMC-OH-N. These results strongly indicate that double-positive charge regulation substantially enhances aqueous solubility and effectively suppresses nonspecific aggregation in aqueous media. We next investigated the pH-dependent spectral behavior of QMC-OH-N. As the pH increased from 5.0 to 10.0, the pH-dependent absorption spectra exhibited a clear bathochromic shift in the maximum absorption wavelength (Fig. S2, from 620 nm to 760 nm). Simultaneously, we observed a substantial decrease in fluorescence intensity at 735 nm (channel 1, λ_{ex} = 620 nm), accompanied by the sharp enhancement of a new NIR emission band centered at 800 nm (channel 2, λ_{ex} = 760 nm, Fig. 2E–G). As shown in Fig. S3, the pK_a constant of the probe was determined to be 5.5, confirming that QMC-OH-N remains in its stable sensing state under physiological conditions. This spectral evolution was attributed to the deprotonation of the phenolic hydroxyl group, which transformed the zwitterionic hydroxyl donor into a potent phenolate anion, thereby strengthening the ICT effect within the quinoline scaffold and causing the observed bathochromic shift in absorption and emission. This dual-channel NIR strategy offers a robust molecular imaging platform, serving as a potent chemical tool for the assessment of infection dynamics.

We then evaluated the *in vivo* pharmacokinetic and liver-targeting efficiency of the quinoline dyes. Following intravenous

injection, QMC-OH-N demonstrated superior liver enrichment and prolonged retention compared to QMC-OH-C and QMC-OH-SO_3 (Fig. 2H). Quantitative analysis of the liver fluorescence showed that QMC-OH-N reached peak intensity at 4 hours post-injection, with a signal approximately 2-fold higher than that of the other two candidates (Fig. 2I). This significantly enhanced liver-targeting capability was mainly attributed to the electrostatic attraction toward the anionic microenvironment (rich in glycosaminoglycans and proteoglycans) of liver tissues. All these spectral and pharmacokinetic results highlight the ability of the dicationic

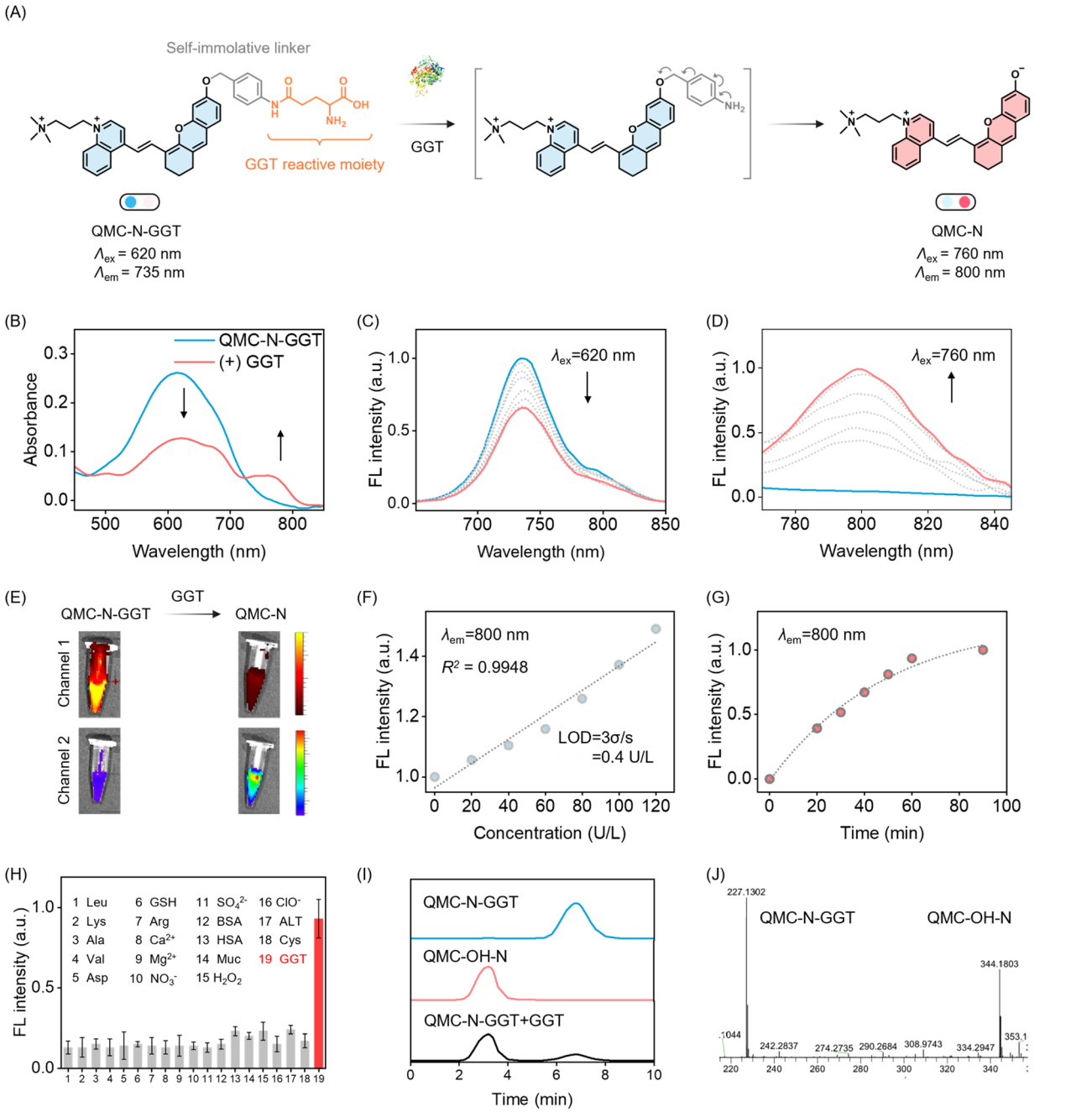

Fig. 3 High-fidelity sensing of GGT *via* dual-channel NIR fluorescence. (A) Schematic illustration of the probe design and the GGT-activated dual-channel fluorescence response. (B) Absorption spectra of QMC-N-GGT (10 μM) in the absence and presence of GGT (120 U L^{-1}). (C and D) Dual-channel NIR fluorescence responses of QMC-N-GGT (10 μM) upon incubation with GGT (120 U L^{-1}). Channel 1: λ_{ex} = 620 nm, λ_{em} = 735 nm (C); and channel 2: λ_{ex} = 760 nm, λ_{em} = 800 nm. (E) Representative macroscopic imaging of QMC-N-GGT (10 μM) before and after GGT (120 U L^{-1}) activation across dual NIR channels (channel 1: λ_{ex} = 620 nm, λ_{em} = 640–750 nm; channel 2: λ_{ex} = 760 nm, λ_{em} = 770–850 nm). (F) Quantitative correlation between the fluorescence intensity at 800 nm and GGT concentrations (0–120 U L^{-1}). (G) Kinetic profiles of the GGT-triggered fluorescence enhancement at 800 nm. (H) Sensing specificity of QMC-N-GGT (10 μM, λ_{ex} = 760 nm, λ_{em} = 800 nm) toward GGT (120 U L^{-1}) compared to various biological interferents. (Leu 1 mM, Lys 1 mM, Ala 1 mM, Val 1 mM, Asp 1 mM, GSH 1 mM, Arg 1 mM, Ca^{2+} 100 μM, Mg^{2+} 100 μM, NO_3^- 100 μM, SO_4^{2-} 100 μM, BSA 100 U L^{-1}, HSA 100 U L^{-1}, Muc 100 U L^{-1}). (I and J) Mechanistic validation *via* HPLC and high-resolution mass spectrometry.

QMC-OH-N to exhibit good water solubility, sensitive dual-channel NIR response,[47–52] and excellent hepatic targeting and retention. We thus envisaged that conjugating a GGT-responsive moiety to this scaffold would yield a dual-channel NIR probe for the real-time *in vivo* monitoring of *Schistosoma* infection.

GGT-triggered dual-channel NIR fluorescence

To implement our sensing strategy, we incorporated the γ-glutamyl-reactive moiety into the phenolic hydroxyl group of the three quinoline-based fluorophores, generating a series of dual-channel NIR probes that bind to GGT: QMC-C-GGT, QMC-SO_3-GGT, and QMC-N-GGT (Fig. 3A and S4). For instance, for QMC-N-GGT, the probe was specifically designed by conjugating a γ-glutamyl moiety to the QMC-OH-N scaffold *via* a *p*-aminobenzyl alcohol-based self-immolative linker. We then carefully evaluated the GGT-triggered spectral response of QMC-N-GGT. Initially, the probe exhibited a strong absorption peak at 620 nm (Fig. 3B). Upon the addition of GGT, a new absorption peak at approximately 735 nm appeared.

This spectral evolution is more obvious in the fluorescence spectra: upon addition of GGT, the fluorescence at 735 nm undergoes a substantial decrease (channel 1, $\lambda_{ex} = 620$ nm), with the concomitant rise of a new NIR emission band peaking at 800 nm (channel 2, $\lambda_{ex} = 760$ nm, Fig. 3C–E). The fluorescence intensity of QMC-N-GGT at 800 nm exhibited a well-defined linear relationship with the GGT concentration in the range of 0–120 U L^{-1}. The calculated LOD of 0.4 U L^{-1} is substantially lower than clinical GGT thresholds, validating the probe's exceptional capability for the sensitive monitoring of hepatic GGT activity (Fig. 3F).

Kinetic analysis revealed that the fluorescence intensity at 800 nm increased and then reached a plateau at approximately 60 min (Fig. 3G). QMC-N-GGT also showed excellent GGT specificity against various species that could potentially compete, including common amino acids, inorganic ions, and biological macromolecules, as well as biologically relevant reactive oxygen species (ROS) and biothiols (Fig. 3H). To ensure the reliability of QMC-N-GGT for persistent bioimaging, we confirmed its superior photostability in comparison with the clinical NIR fluorophore ICG (Fig. S5). These results highlighted the sensitivity and selectivity of QMC-N-GGT with a GGT-triggered dual-channel NIR fluorescence response.

To further validate the proposed sensing mechanism, we conducted a comprehensive analysis using high-performance liquid chromatography (HPLC) and mass spectrometry (MS). As shown in Fig. 3I, the QMC-N-GGT probe exhibited a single characteristic peak at a retention time of 6.8 min. Upon incubation with GGT, a distinct new peak emerged at 3.2 min, which precisely aligned with the retention time of the independently synthesized active fluorophore QMC-OH-N. The ESI-MS spectrum of QMC-N-GGT incubated with GGT for 60 min showed an observed *m*/*z* of 227.1302 and 344.1803 (Fig. 3J), corresponding to the hypothesized product QMC-OH-N and the probe QMC-N-GGT, respectively. The dual-channel NIR fluorescence of QMC-N-GGT made it possible to ratio metrically track when, where,

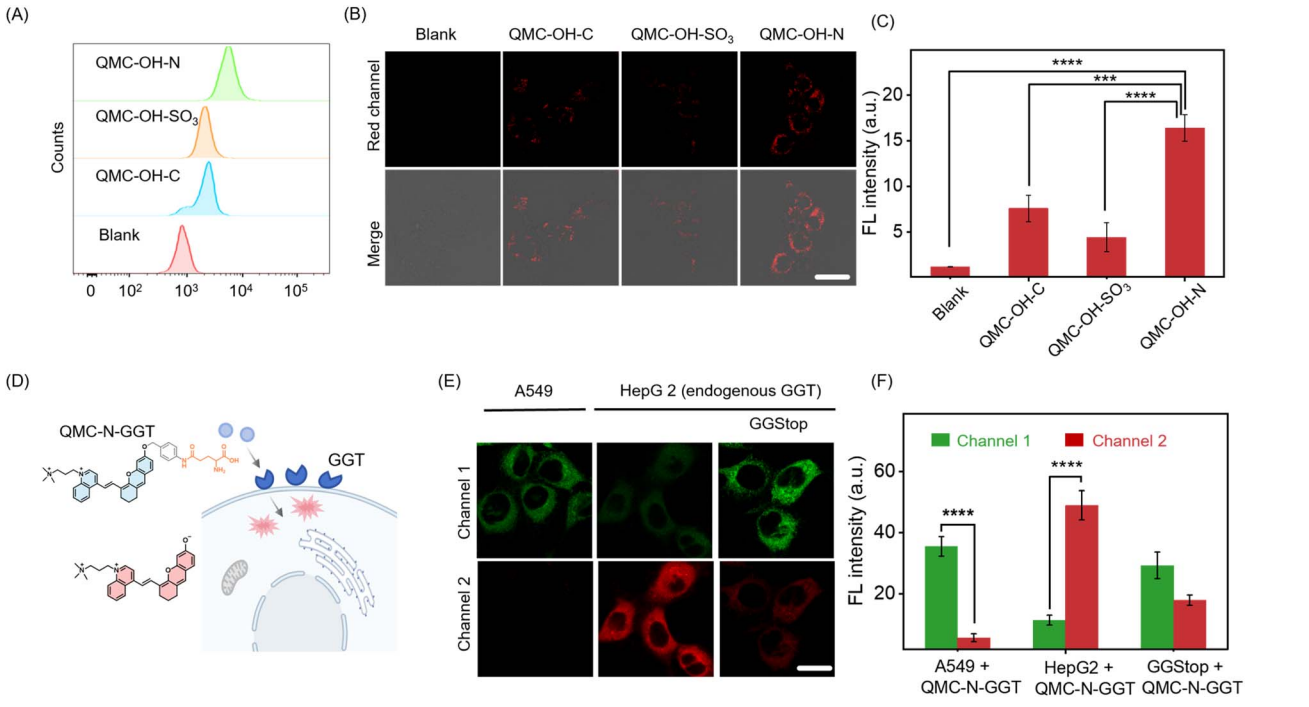

Fig. 4 Endogenous GGT-activatable fluorescence. (A) Flow cytometry analysis of HepG2 cells incubated with QMC-OH-C, QMC-OH-SO_3, and QMC-OH-N (10 μM). (B and C) Confocal laser scanning microscopy images (B) and corresponding mean fluorescence intensity (C) of HepG2 cells treated with the three probes ($\lambda_{ex} = 620$ nm, $\lambda_{em} = 640–750$ nm). Scale bar: 20 μm. ****$P < 0.0001$ by unpaired two-tailed Student's *t*-test. (D and E) High-contrast imaging of endogenous GGT activity in different cell lines (QMC-OH-N 10 μM, channel 1: $\lambda_{ex} = 620$ nm, $\lambda_{em} = 640–750$ nm; channel 2: $\lambda_{ex} = 760$ nm, $\lambda_{em} = 770–850$ nm). Scale bar: 20 μm. (F) Quantitative fluorescence intensity of Channel 1 and Channel 2 across each group in panel E. ****$P < 0.0001$.

and how the probe targets the liver (channel 1) and illuminates endogenous GGT *in situ* (channel 2).

Dual-channel NIR fluorescence tracking of endogenous GGT in living cells

To investigate the capability of QMC-N-GGT to track endogenous GGT activity, we examined its dual-channel fluorescence responses in living cells. We first assessed the cellular internalization of the fluorophore engineered with different charge properties. Flow cytometry analysis indicated that double-positive-charged QMC-OH-N exhibited a pronounced rightward shift in fluorescence counts compared to the zwitterionic alkyl-substituted QMC-OH-C and the anionic QMC-OH-SO_3 derivatives (Fig. 4A).

This superior internalization was visually confirmed by confocal laser scanning microscopy, where QMC-OH-N-treated cells displayed the brightest and most uniform intracellular staining (Fig. 4B and C). Cytotoxicity assays in HepG2 and 293T cell lines confirmed that QMC-N-GGT exhibited negligible toxic effects (Fig. S6), demonstrating satisfactory biocompatibility for cellular sensing and imaging. Cell retention and co-localization assays further indicated that the dicationic structure effectively prevented probe efflux through enhanced electrostatic interactions (Fig. S7 and S8).

We next evaluated the intracellular sensing performance of the GGT-responsive probe QMC-N-GGT (Fig. 4D). In A549 cells (a GGT-underexpressing cell line), fluorescence was primarily observed in channel 1 (735 nm, Fig. 4E). In contrast, HepG2 cells (GGT-overexpressing)[53,54] showed a decrease in channel 1 signal and a significant increase in channel 2 emission (800 nm, Fig. 4E), confirming probe activation by endogenous GGT. To further verify the specificity, we incubated HepG2 cells with GGStop (a GGT inhibitor). As expected, this treatment suppressed the fluorescence increase at 800 nm, and the resulting signal levels were directly correlated with cellular GGT activity (Fig. 4E and F). These results highlighted that QMC-N-GGT combined efficient cellular uptake, satisfactory biocompatibility, and a specific dual-channel fluorescence response to endogenous GGT. Thus, QMC-N-GGT provides a reliable method for visualizing enzymatic activity in living cells, and offers a promising tool for tracking GGT-relevant biological processes, especially *Schistosoma* infection.

Double-positive charge strategy enabling *in situ* identification of *Schistosoma* infection *via* illuminating hepatic GGT

Based on the promising cellular GGT imaging performance, we then assessed the potential of QMC-N-GGT for *in vivo* identification of *Schistosoma* infection *via* probing hepatic GGT. The pathology of schistosomiasis is characterized by the maturation of cercariae into adults, which triggers an intense inflammatory cascade and subsequent aberrant GGT upregulation during hepatic fibrosis. To model this, mice were percutaneously infected with cercariae following standardized protocols, leading to significant hepatic architectural remodeling (Fig. 5A).

We then investigated the *in vivo* imaging performance by comparing the three charge-tailored probes (QMC-C-GGT, QMC-SO_3-GGT, and QMC-N-GGT) in healthy and infected mice following intravenous injection. The distribution and activation of each probe were tracked *via* channel 1 (yellow-red) and 2 (rainbow) fluorescence readouts, respectively (Fig. 5B–G). In healthy mice, the hepatic fluorescence intensity of QMC-N-GGT progressively increased after injection, reaching a maximum at 4 hours post-injection (Fig. 5B and C). This was followed by a gradual metabolic clearance, with a noticeable decrease in signal intensity at 16 hours. Notably, at the peak time point (4 h), the liver signal from the dicationic QMC-N-GGT was substantially stronger than that of its single-positive-charged QMC-C-GGT or zwitterionic QMC-SO_3-GGT (Fig. 5D).

To ensure the reliability of this approach in complex internal environments, we validated the stability of the reference signal (channel 1). As shown in Fig. S9, the fluorescence intensity of channel 1 remained highly stable across a wide physiological pH range (pH 4.0–9.0), confirming its photophysical stability to local pH fluctuations. Furthermore, zeta potential measurements (Fig. S10) revealed that QMC-N-GGT maintained a significantly positive charge (approximately 12 mV) even after incubation with 50% fetal bovine serum (FBS), indicating that the dicationic scaffold is not completely shielded by protein corona formation. This result strongly indicates that the double-positive-charge strategy can effectively promote liver enrichment and retention.

In *Schistosoma*-infected mice, the activated form of QMC-N-GGT produced much stronger fluorescence in channel 2 (at the liver site), along with a weak signal in channel 1 (Fig. 5E). This was attributed to the GGT-triggered activation in the liver. This response was significantly more pronounced with QMC-N-GGT than with the other two probes, yielding the highest signal-to-noise ratio for detecting *Schistosoma* infection (Fig. 5F and G). Biodistribution analysis of major organs collected 24 hours post-injection showed that all three probes were primarily localized in the liver, with weaker signals in the kidneys and negligible fluorescence in the heart, spleen, and lungs (Fig. 5H and I). Consistent with the real-time imaging data, QMC-N-GGT exhibited the highest hepatic fluorescence intensity in channel 1 and 2 (in isolated liver, Fig. 5J and K), further supporting its superior liver-targeting and GGT-sensing capability.

Histological examination (H&E staining) of organs from healthy mice treated with QMC-N-GGT revealed no apparent morphological damage or inflammatory infiltration compared to the PBS control group (Fig. S11), indicating satisfactory biocompatibility *in vivo*. All these *in vivo* results demonstrate that double-positive-charged QMC-N-GGT integrates excellent liver-targeting properties with the capacity for real-time, specific visualization of GGT upregulation. This enables intact diagnosis of *Schistosoma* infection during its pathological progression, highlighting the potential of double-positive-charged QMC-N-GGT as a precision imaging tool for staging *Schistosoma* infection.

Intact tracking of the spatiotemporal progression: staging *Schistosoma* infection in living mice

The dual-channel response and hepatic targeting capability of QMC-N-GGT inspired us to further explore its utility for staged diagnosis of *Schistosoma* infection progression. With this in

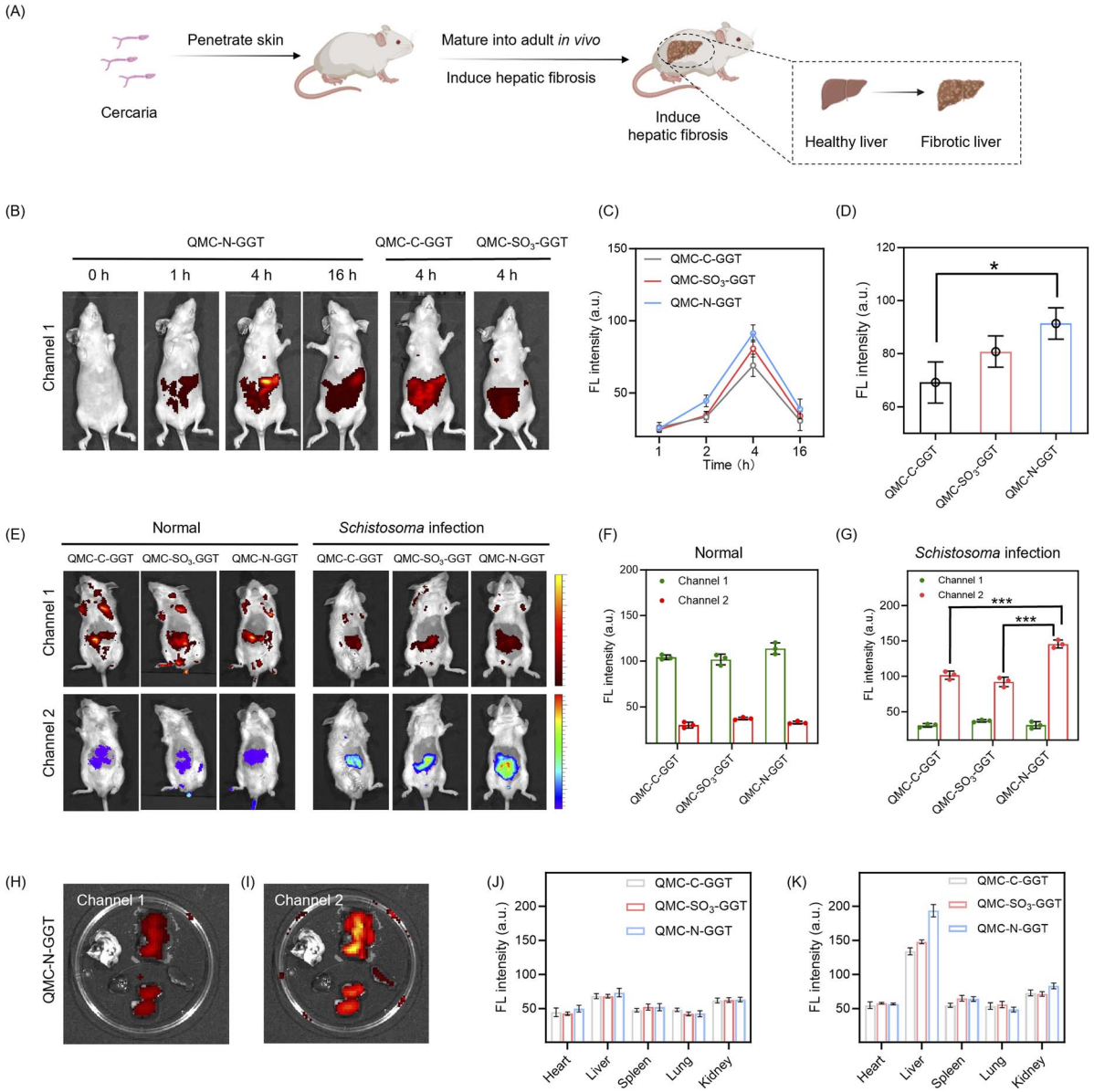

Fig. 5 Dual Channel GGT detection enabling *in vivo* mapping *Schistosoma*-infection. (A) Schematic illustration of the *Schistosoma*-infectious mouse model establishment. (B) *In vivo* NIR fluorescence imaging of healthy mice of the three probes (100 μM, channel 1: $\lambda_{ex} = 620$ nm, $\lambda_{em} =$ 640–750 nm). (C and D) Quantitative comparison of total fluorescence intensity (Channel 1) in the liver regions of healthy mice. ****$P < 0.0001$ by unpaired two-tailed Student's *t*-test. (E) *In vivo* dual-channel NIR fluorescence imaging of healthy and infected mice one hour after intravenous injection of the three probes. (F and G) Statistical analysis of fluorescence signals in Channel 1 and Channel 2 for three probes in normal (F) and infectious (G) mice (100 μM, channel 1: $\lambda_{ex} = 620$ nm, $\lambda_{em} = 640–750$ nm; channel 2: $\lambda_{ex} = 760$ nm, $\lambda_{em} = 770–850$ nm). ****$P < 0.0001$. (H and I) *Ex vivo* fluorescence images of major organs (heart, liver, spleen, lung, and kidney) in channel 1 (H) and channel 2 (I) at 24 h post-injection, confirming the specific activation in liver tissue. (J and K) Quantitative biodistribution (J, channel 1) and activation analysis (J, channel 2) in major organs for the three probes.

mind, we systematically monitored the pathological progression of hepatic fibrosis induced by *Schistosoma japonicum* infection in a murine model (Fig. 6A). According to the experimental timeline, the infection progressed from initial percutaneous exposure on day 0 to severe pathology by day 40. To correlate the probe's fluorescence response with the actual physiological state, histopathological analysis was performed using H&E and Masson's trichrome staining.[55–57] The H&E sections revealed progressive hepatic structural disorganization and inflammatory infiltration (marked in Fig. 6B), while the Masson's trichrome staining clearly depicted the severity-dependent deposition of collagen in the liver (blue regions in Fig. 6C). These results confirmed the transition from a healthy liver to the slight, moderate, and severe infection states, thereby providing a robust biochemical basis for our GGT-responsive imaging using QMC-N-GGT.

Subsequently, *in vivo* fluorescence imaging was employed to track the real-time activation of the probe across varying

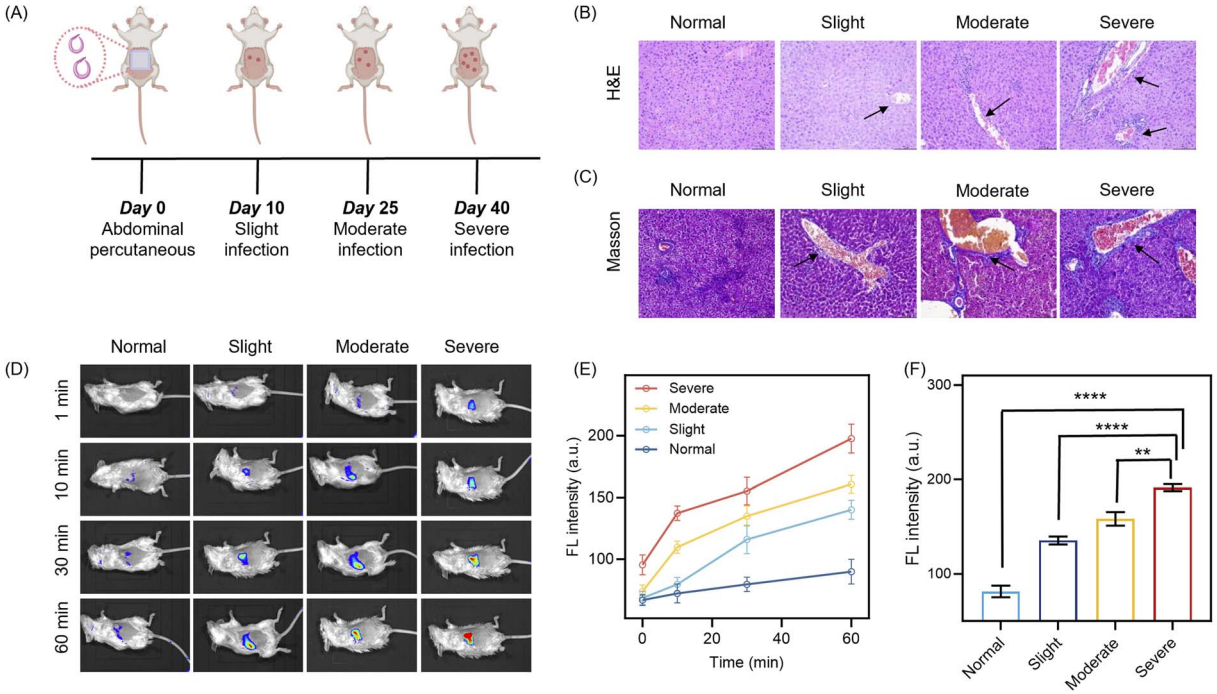

Fig. 6 Staging of *Schistosoma*-infection *via* NIR imaging. (A) Schematic illustration of the *Schistosoma*-infectious mouse model establishment, depicting the timeline from abdominal percutaneous infection (day 0) to severe hepatic fibrosis (day 40). (B and C) Representative histopathological images of liver sections from mice at distinct stages of *Schistosoma*-infection (normal, slight, middle, and severe). HE staining (B) shows normal hepatic tissue (pink) and an area of inflammatory lesions (purplish-blue). Tissue disruption due to the lesion is indicated by the black arrow. Masson's trichrome staining (C) shows normal liver tissue (pink) and areas of hepatic fibrosis (blue), with bridging fibrosis forming fibrous septa (black arrow). (D) Time-dependent *in vivo* NIR fluorescence imaging (1, 10, 30, and 60 min) of infectious mice following intravenous injection of QMC-N-GGT (100 μM, λ_{ex} = 760 nm, λ_{em} = 770–850 nm). (E) Kinetic plots of average fluorescence intensity at the liver site as a function of time (0–60 min) across the four groups, demonstrating stage-dependent activation rates. (F) Statistical comparison of the total fluorescence intensity at the liver site at 60 min post-injection, confirming the probe's ability to differentiate the severity of schistosomiasis. Data are expressed as mean ± s.d. (n = 3). ****P < 0.0001 by unpaired two-tailed Student's t-test.

infection stages (normal, slight, moderate, and severe, Fig. 6D). Following intravenous administration of QMC-N-GGT in the healthy group, no significant fluorescence enhancement (channel 2) was observed, demonstrating the remarkably low background and excellent stability of QMC-N-GGT against non-specific activation. In contrast, infected mice showed a rapid and substantial signal increase at 800 nm, with the fluorescence intensity positively correlated with the infection severity.

Kinetic profiles further characterized the response of the probe toward varying levels of *Schistosoma* infection. Although fluorescence continuously increased over 60 minutes in all groups, the fluorescent response kinetics and intensity level were markedly different among the severity stages (Fig. 6E and F). Specifically, the severe infection group displayed the fastest activation kinetics and the highest final signal. Quantitative analysis confirmed this severity-dependent trend: the average fluorescence intensity at the 60-minute time points increased stepwise from the slight to severe infection groups, with all infected stages showing a statistically significant enhancement (p < 0.001) compared to the normal control. Thus, QMC-N-GGT successfully transduced the pathological progression of *Schistosoma* infection into a severity-dependent NIR signal with a high spatiotemporal resolution. These results establish this probe as a powerful diagnostic tool for the *in situ* mapping and staging of schistosomiasis.

Conclusions

We developed a rational molecular engineering strategy to address the critical bottleneck in non-invasive staging of *Schistosoma* infection, which remains challenging for conventional anatomical imaging. Unlike traditional microscopic examination and ultrasonographic diagnostic modalities limited by sensitivity or late stage detection, our approach focuses on the precise charge-regulation of a quinoline scaffold to optimize the *in vivo* pharmacokinetics of probes for dual-channel ratiometric sensing. Specifically, by manipulating the fluorophore core from zwitterionic, single-positive charge, to double-positive charge, the optimized probe QMC-N-GGT achieves significant enhancement in hepatic accumulation *via* electrostatic recruitment to the anionic fibrotic microenvironment.

Leveraging this hepatotropic targeting and a GGT-activatable dual-channel ratiometric mechanism, QMC-N-GGT enables high-fidelity visualization of enzymatic dynamics with a remarkable signal-to-noise ratio. We established a mouse model of *Schistosoma* infection *via* standard protocol. Crucially, the probe successfully decodes the spatiotemporal evolution of *Schistosoma* infection, accurately differentiating slight, moderate, and severe stages through distinct fluorescence kinetic profiles, a capability previously unattainable with real-time *in vivo* settings. This study not only provides a potent

chemical tool for the precise evolutionary staging of parasitic diseases, but also establishes a generalized paradigm for designing charge-regulated molecular probes to interrogate complex deep-tissue pathologies in clinical translation.

Ethical statement

All animal procedures were performed in accordance with the Guidelines for Care and Use of Laboratory Animals of East China University of Science and Technology (ECUST-2023-026) and approved by the Institutional Animal Care and Use Committee of the National Tissue Engineering Center (Shanghai, China).

Author contributions

All the experiments were conducted by X. M., E. X., Q. L., C. S., and Y. Y., with the supervision of C. Y., Q. L., W. Z., and Z. G. All the authors analyzed the data and contributed to the manuscript writing.

Conflicts of interest

The authors declare no competing financial interests.

Data availability

The supporting data have been included in the article's supplementary information (SI). All data generated and analyzed during the study are available from the corresponding authors on reasonable request. Supplementary information: NMR spectra of synthesized compounds, spectroscopic data of the probes, and supplementary cellular experimental results. See DOI: https://doi.org/10.1039/d6sc02037b.

Acknowledgements

This work was supported by the National Key Research and Development Program (2023YFA1802000), NSFC/China (22225805, 32121005, T2522013, 32394001, and 22378122), Shanghai Science and Technology Innovation Action Plan (No. 23J21901600), Innovation Program of the Shanghai Municipal Education Commission, Shanghai Frontier Science Research Base of Optogenetic Techniques for Cell Metabolism (Shanghai Municipal Education Commission, Grant 2021 Sci & Tech 0328), the Science and Technology Commission of Shanghai Municipality (24DX1400200), and the Fundamental and Interdisciplinary Disciplines Breakthrough Plan of the Ministry of Education of China (JYB2025XDXM404).

Notes and references

1 B. Gryseels, K. Polman, J. Clerinx and L. Kestens, Human schistosomiasis, *Lancet*, 2006, **368**(9541), 1106–1118.
2 E. L. Houlder, K. A. Stam, J. P. R. Koopman, M. H. König, M. C. C. Langenberg, M. A. Hoogerwerf, P. Niewold, F. Sonnet, J. J. Janse, M. C. Partal, J. C. Sijtsma, L. H. M. de Bes-Roeleveld, Y. C. M. Kruize, M. Yazdanbakhsh and M. Roestenberg, Early symptom-associated inflammatory responses shift to type 2 responses in controlled human schistosome infection, *Sci. Immunol.*, 2024, **9**(97), eadl1965.
3 Y. You, S. Cheng, X. Chen, X. Chen, C. Yi, M. Cai, F. Luo, X. Wang, Y. Xie, W. Yang, L. Xiu, M. Gu, C. Sun, L. Huo, G. Chen, S. Li, J. Wang and W. Hu, Dynamic single-cell transcriptomics reveals lsamp-guided neural network formation in male S. japonicum driving female reproduction, *Nat. Commun.*, 2026, **17**(1), 1602.
4 N. C. Lo, F. S. M. Bezerra, D. G. Colley, F. M. Fleming, M. Homeida, N. Kabatereine, F. M. Kabole, C. H. King, M. A. Mafe, N. Midzi, F. Mutapi, J. R. Mwanga, R. M. R. Ramzy, F. Satrija, J. R. Stothard, M. S. Traoré, J. P. Webster, J. Utzinger, X. N. Zhou, A. Danso-Appiah, P. Eusebi, E. S. Loker, C. O. Obonyo, R. Quansah, S. Liang, M. Vaillant, M. H. Murad, P. Hagan and A. Garba, Review of 2022 WHO guidelines on the control and elimination of schistosomiasis, *Lancet Infect. Dis.*, 2022, **22**(11), e327–e335.
5 M. C. C. Langenberg, M. A. Hoogerwerf, J. P. R. Koopman, J. J. Janse, J. Kos-van Oosterhoud, C. Feijt, S. P. Jochems, C. J. de Dood, R. van Schuijlenburg, A. Ozir-Fazalalikhan, M. D. Manurung, E. Sartono, M. T. van der Beek, B. M. F. Winkel, P. H. Verbeek-Menken, K. A. Stam, F. W. B. van Leeuwen, P. Meij, A. van Diepen, L. van Lieshout, G. J. van Dam, P. Corstjens, C. H. Hokke, M. Yazdanbakhsh, L. G. Visser and M. Roestenberg, A controlled human Schistosoma mansoni infection model to advance novel drugs, vaccines and diagnostics, *Nat. Med.*, 2020, **26**(3), 326–332.
6 J. P. R. Koopman, E. L. Houlder, J. J. Janse, O. A. Lamers, G. V. Roozen, J. C. Sijtsma, M. Casacuberta-Partal, S. T. Hilt, M. van der Stoep, I. M. van Amerongen-Westra, E. A. Brienen, L. J. Wammes, L. van Lieshout, G. J. van Dam, P. L. Corstjens, A. van Diepen, M. Yazdanbakhsh, C. H. Hokke and M. Roestenberg, Clinical tolerance but no protective efficacy in a placebo-controlled trial of repeated controlled schistosome infection, *J. Clin. Invest.*, 2024, **135**(4).
7 J. Rivera, Y. Mu, C. A. Gordon, M. K. Jones, G. Cheng and P. Cai, Current and upcoming point-of-care diagnostics for schistosomiasis, *Trends Parasitol.*, 2024, **40**(1), 60–74.
8 D. J. Berger, T. Crellen, P. H. L. Lamberton, F. Allan, A. Tracey, J. D. Noonan, N. B. Kabatereine, E. M. Tukahebwa, M. Adriko, N. Holroyd, J. P. Webster, M. Berriman and J. A. Cotton, Whole-genome sequencing of Schistosoma mansoni reveals extensive diversity with limited selection despite mass drug administration, *Nat. Commun.*, 2021, **12**(1), 4776.
9 B. Zhang, J. Lu, X. Lin, J. Wang, Q. Li, T. Jin, Q. Shi, Y. Lu, J. Zhang, J. Deng, Y. Zhang, Y. Guo, J. Gao, H. Chen, Y. Yan, J. Wu, J. Gao, J. Che, X. Dong, Z. Gu and N. Lin, Injectable and sprayable fluorescent nanoprobe for rapid real-time detection of human colorectal tumors, *Adv. Mater.*, 2024, **36**(36), e2405275.
10 H. Li, D. Kim, Q. Yao, H. Ge, J. Chung, J. Fan, J. Wang, X. Peng and J. Yoon, Activity-based NIR enzyme fluorescent

probes for the diagnosis of tumors and image-guided surgery, *Angew. Chem., Int. Ed.*, 2021, **60**(32), 17268–17289.
11 X. Wang, Q. Ding, R. R. Groleau, L. Wu, Y. Mao, F. Che, O. Kotova, E. M. Scanlan, S. E. Lewis, P. Li, B. Tang, T. D. James and T. Gunnlaugsson, Fluorescent probes for disease diagnosis, *Chem. Rev.*, 2024, **124**(11), 7106–7164.
12 S. Cao, C. Sun, X. Y. Zhang, C. Yoon, Z. Liu, J. Yoo, Y. Kim, X. Yu, Y. Xu, J. S. Kim and K. N. Wang, Real-time super-resolution tracking of mtDNA remodeling and inflammatory release with a selective fluorescent probe, *Angew. Chem., Int. Ed.*, 2026, **65**(7), e20934.
13 K. Fujita, M. Kamiya, T. Yoshioka, A. Ogasawara, R. Hino, R. Kojima, H. Ueo and Y. Urano, Rapid and accurate visualization of breast tumors with a fluorescent probe targeting α-mannosidase 2C1, *ACS Cent. Sci.*, 2020, **6**(12), 2217–2227.
14 J. Han, M. Yang, C. Lv, K. Li, J. Fan and X. Peng, A unimolecular near-infrared fluorescent probe for in vivo imaging of enzymes with minimized false-negative signals, *Chem. Sci.*, 2026, **17**(5), 2791–2801.
15 L. Wu, Z. Li, K. Wang, R. R. Groleau, X. Rong, X. Liu, C. Liu, S. E. Lewis, B. Zhu and T. D. James, Advances in organic small molecule-based fluorescent probes for precision detection of liver diseases: a perspective on emerging trends and challenges, *J. Am. Chem. Soc.*, 2025, **147**(11), 9001–9018.
16 Y. Mao, W. Zhang, X. Wang, P. Li and B. Tang, Rational design of fluorescent imaging agents for hepatic diseases: from molecular mechanisms to diagnostic precision, *Chem. Soc. Rev.*, 2026, **55**, 4121–4159.
17 T. Xia, Z. Xia, P. Tang, J. Fan and X. Peng, Light-driven mitochondrion-to-nucleus DNA cascade fluorescence imaging and enhanced cancer cell photoablation, *J. Am. Chem. Soc.*, 2024, **146**(19), 12941–12949.
18 X. Wu, F. Xing, Y. Yang, X. Liu, G. Kim, Q. Jiang, Y. Xu, J. J. Hu, G. Liang and J. Yoon, Caged ligand-decorated near-infrared photosensitizer with in vivo albumin-hijacking capacity for tumor-targeted hypoxia-tolerant photoimmunotherapy of cancer, *J. Am. Chem. Soc.*, 2026, **148**(6), 6135–6147.
19 Y. Tang, Y. Li, C. He, Z. Wang, W. Huang, Q. Fan and B. Liu, NIR-II-excited off-on-off fluorescent nanoprobes for sensitive molecular imaging in vivo, *Nat. Commun.*, 2025, **16**(1), 278.
20 H. Wang, X. Zhang, P. Li, F. Huang, T. Xiu, H. Wang, W. Zhang, W. Zhang and B. Tang, Prediction of early atherosclerotic plaques using a sequence-activated fluorescence probe for the simultaneous detection of γ-glutamyl transpeptidase and hypobromous acid, *Angew. Chem., Int. Ed.*, 2024, **63**(1), e202315861.
21 R. An, S. Wei, Z. Huang, F. Liu and D. Ye, An activatable chemiluminescent probe for sensitive detection of γ-glutamyl transpeptidase activity in vivo, *Anal. Chem.*, 2019, **91**(21), 13639–13646.
22 S. Wang, D. Lian, C. Sun, M. Xu, M. Zhu, C. Yan and Z. Guo, High selective NIR-II fluorescent probe for sensing phosgene in plants, *Chin. Chem. Lett.*, 2025, **37**(7), 111744.
23 B. Dai, S. Huang, Q. Hu, P. Wang, L. Gong, G. Xu, F. Wu, H. Qin, S. Xia, W. Sun, H. Li, Z. Feng, C. Ren, J. Shen and M. Liu, Circular RNA Gsr-0002 promotes schistosomiasis-induced liver fibrosis by regulating the DNMT3A/PTEN pathway, *Int. J. Biol. Macromol.*, 2025, **333**(Pt 1), 148776.
24 X. He, Y. Sun, N. Lei, X. Fan, C. Zhang, Y. Wang, K. Zheng, D. Zhang and W. Pan, MicroRNA-351 promotes schistosomiasis-induced hepatic fibrosis by targeting the vitamin D receptor, *Proc. Natl. Acad. Sci. U. S. A.*, 2018, **115**(1), 180–185.
25 K. Li, Y. Lyu, Y. Huang, S. Xu, H. W. Liu, L. Chen, T. B. Ren, M. Xiong, S. Huan, L. Yuan, X. B. Zhang and W. Tan, A de novo strategy to develop NIR precipitating fluorochrome for long-term in situ cell membrane bioimaging, *Proc. Natl. Acad. Sci. U. S. A.*, 2021, **118**(8), e2018033118.
26 H. Wang, X. Zhang, P. Li, F. Huang, T. Xiu, H. Wang, W. Zhang, W. Zhang and B. Tang, Prediction of early atherosclerotic plaques using a sequence-activated fluorescence probe for the simultaneous detection of γ-glutamyl transpeptidase and hypobromous acid, *Angew. Chem., Int. Ed.*, 2024, **63**(1), e202315861.
27 M. Zhao, Y. Lu, Y. Zhang, H. Xue and Z. Guo, Ultra-high signal-to-noise ratio near-infrared chemiluminescent probe for *in vivo* sensing singlet oxygen, *Chin. Chem. Lett.*, 2025, **36**(5).
28 H. Bian, D. Ma, F. Pan, X. Zhang, K. Xin, X. Zhang, Y. Yang, X. Peng and Y. Xiao, Cardiolipin-targeted NIR-II fluorophore causes "avalanche effects" for re-engaging cancer apoptosis and inhibiting metastasis, *J. Am. Chem. Soc.*, 2022, **144**(49), 22562–22573.
29 L. Chen, Y. He, J. Lan, Z. Li, D. Gu, W. Nie, T. Zhang and Y. Ding, Advancements in nano drug delivery system for liver cancer therapy based on mitochondria-targeting, *Biomed. Pharmacother.*, 2024, **180**, 117520.
30 M. Chang, C. Yan, L. Shi, D. Li, W. Fu and Z. Guo, Rational design of shortwave infrared (SWIR) fluorescence probe: Cooperation of ICT and ESIPT processes for sensing endogenous cysteine, *Chin. Chem. Lett.*, 2022, **33**(2), 762–766.
31 D. Zhang, K. X. Teng, N. Shao, L. Y. Niu and Q. Z. Yang, Cascade responsive photosensitizer for precise delivery and photodynamic therapy, *J. Med. Chem.*, 2025, **68**(8), 8648–8658.
32 X. Zhang, S. Shen, D. Liu, X. Li, W. Shi and H. Ma, Combination of changeable π-conjugation and hydrophilic groups for developing water-soluble small-molecule NIR-II fluorogenic probes, *Chem. Sci.*, 2023, **14**(11), 2928–2934.
33 N. Li, Z. Liu, C. Chen, H. Jiang, Y. Liu and D. Ni, Activatable fluorescent ratiometric probes for early diagnosis and prognostic assessment of acute kidney injury, *Sci. Adv.*, 2025, **11**(43), eaea1654.
34 Y. Zhang, X. Chen, Q. Yuan, Y. Bian, M. Li, Y. Wang, X. Gao and D. Su, Enzyme-activated near-infrared fluorogenic probe with high-efficiency intrahepatic targeting ability for visualization of drug-induced liver injury, *Chem. Sci.*, 2021, **12**(44), 14855–14862.
35 Q. Zhou, S. Shao, J. Wang, C. Xu, J. Xiang, Y. Piao, Z. Zhou, Q. Yu, J. Tang, X. Liu, Z. Gan, R. Mo, Z. Gu and Y. Shen,

Enzyme-activatable polymer-drug conjugate augments tumour penetration and treatment efficacy, *Nat. Nanotechnol.*, 2019, **14**(8), 799–809.

36 Z. Ye, C. Qiu, Z. Liu, H. Wen, F. Gao, Y. Zhang, W. J. Wang, J. Zhang, Z. Qiu, W. Zhang, P. Alam, Z. Zhao and B. Z. Tang, Counterion-driven long-term imaging of cell membranes and migrasomes using dicationic NIR AIEgens, *J. Am. Chem. Soc.*, 2025, **147**(31), 28442–28453.

37 J. Miao, Y. Huo, G. Yao, Y. Feng, J. Weng, W. Zhao and W. Guo, Heavy atom-free, mitochondria-targeted, and activatable photosensitizers for photodynamic therapy with real-time in-situ therapeutic monitoring, *Angew. Chem., Int. Ed.*, 2022, **61**(25), e202201815.

38 J. Zuo, A. Peng, P. Wu, J. Chen, C. Yao, J. Pan, E. Zhu, Y. Weng, K. Zhang, H. Feng, Z. Jin and Z. Qian, Charge-regulated fluorescent anchors enable high-fidelity tracking of plasma membrane dynamics during biological events, *Chem. Sci.*, 2024, **15**(23), 8934–8945.

39 J. Zhang, Y. Hu, X. Wen, Z. Yang, Z. Wang, Z. Feng, H. Bai, Q. Xue, Y. Miao, T. Tian, P. Zheng, J. Zhang, J. Li, L. Qiu, J. J. Xu and D. Ye, Tandem-controlled lysosomal assembly of nanofibres induces pyroptosis for cancer immunotherapy, *Nat. Nanotechnol.*, 2025, **20**(4), 563–574.

40 A. Radmand, H. Kim, J. Beyersdorf, C. N. Dobrowolski, R. Zenhausern, K. Paunovska, S. G. Huayamares, X. Hua, K. Han, D. Loughrey, M. Z. C. Hatit, A. Del Cid, H. Ni, A. Shajii, A. Li, A. Muralidharan, H. E. Peck, K. E. Tiegreen, S. Jia, P. J. Santangelo and J. E. Dahlman, Cationic cholesterol-dependent LNP delivery to lung stem cells, the liver, and heart, *Proc. Natl. Acad. Sci. U. S. A.*, 2024, **121**(11), e2307801120.

41 C. Yan, C. Liu, B. Liu, Q. Zheng, X. Zhao, S. Lu, X. Fu, W. Li, J. Li, D. Li, Y. Yao, Y. Zhang, H. Zhu, P. Shi, W. H. Zhu and Z. Guo, Fluorescence lifetime clocks quantify senescence and aging, *Nat. Aging*, 2025, **5**(12), 2532–2545.

42 Y. Yao, J. Chen, C. Yan, M. Gao, J. Liu, W. H. Zhu, C. Fan and Z. Guo, Excitation-matchable shortwave infrared quinolinium fluorophores: decoding spatiotemporal interactions with multiplexed bioimaging, *J. Am. Chem. Soc.*, 2025, **147**(51), 46953–46965.

43 Q. Liu, Z. Li, Y. Huang, Z. Lin, X. C. Shen and H. Chen, Deep-NIR to NIR-II hemicyanine fluorophore scaffolds with dual optically tunable sites for *in vivo* multiplexed imaging, *Chem. Sci.*, 2025, **16**(48), 23394–23404.

44 H. Yang, D. Li, J. Wu and K. Pu, Shortwave infrared hemicyanine-6 for cancer-activated and shaving-free preclinical imaging of lung metastasis, *J. Am. Chem. Soc.*, 2025, **147**(34), 30794–30802.

45 W. Fan, K. Adebowale, L. Vancza, Y. Li, M. F. Rabbi, K. Kunimoto, D. Chen, G. Mozes, D. K. Chiu, Y. Li, J. Tao, Y. Wei, N. Adeniji, R. L. Brunsing, R. Dhanasekaran, A. Singhi, D. Geller, S. H. Lo, L. Hodgson, E. G. Engleman, G. W. Charville, V. Charu, S. P. Monga, T. Kim, R. G. Wells, O. Chaudhuri and N. J. Torok, Matrix viscoelasticity promotes liver cancer progression in the pre-cirrhotic liver, *Nature*, 2024, **626**(7999), 635–642.

46 A. M. Nicoli and M. S. Frei, Synthetic fluorophores for live-cell fluorescence microscopy and biosensing, *Nat. Chem. Biol.*, 2025, **21**(12), 1846–1858.

47 X. Wang, S. S. Liew, J. Huang, Y. Hu, X. Wei and K. Pu, Dual-locked enzyme-activatable bioorthogonal fluorescence turn-on imaging of senescent cancer cells, *J. Am. Chem. Soc.*, 2024, **146**(32), 22689–22698.

48 Y. Ma, C. Yan, Z. Guo, G. Tan, D. Niu, Y. Li and W. H. Zhu, Spatio-temporally reporting dose-dependent chemotherapy via uniting dual-modal MRI/NIR imaging, *Angew. Chem., Int. Ed.*, 2020, **59**(47), 21143–21150.

49 C. Yan, Z. Guo, Y. Liu, P. Shi, H. Tian and W. H. Zhu, A sequence-activated and logic dual-channel fluorescent probe for tracking programmable drug release, *Chem. Sci.*, 2018, **9**(29), 6176–6182.

50 H. Meng, J. Wang, H. Wen, Z. Xu, L. Luo, W. Lin, K. Lu, Y. Lu, J. Wang, Y. Xiong, J. Xu, Z. W. Mao and W. Xia, Evoking simultaneous ferroptosis and apoptosis by a dual-locked platinum (IV) prodrug for synergistic chemo-immunotherapy, *Angew. Chem., Int. Ed.*, 2025, **64**(28), e202505930.

51 F. Chu, B. Feng, Y. Zhou, M. Liu, H. Zhang, M. Liu, Q. Chen, S. Zhang, Y. Ma, J. Dong, F. Chen and W. Zeng, Debut of enzyme-responsive anionic cyanine for overlap-free NIR-II-to-I dual-channel tumour imaging, *Chem. Sci.*, 2025, **16**(10), 4490–4500.

52 W. Liu, B. Huang, Z.-X. Tong, S. Wang, Y.-J. Li and Y.-Y. Dai, A sensitive two-photon ratiometric fluorescent probe for γ-glutamyltranspeptidase activity detection and imaging in living cells and cancer tissues, *New J. Chem.*, 2018, **42**(7), 5403–5407.

53 H. Hino, M. Kamiya, K. Kitano, K. Mizuno, S. Tanaka, N. Nishiyama, K. Kataoka, Y. Urano and J. Nakajima, Rapid Cancer Fluorescence Imaging Using A γ-glutamyltranspeptidase-specific probe for primary lung cancer, *Transl. Oncol.*, 2016, **9**(3), 203–210.

54 Q. Wu, H. M. O'Connor and D. M. Elston, Retrospective analysis of Verhoeff-Van Gieson elastic staining, diffractive microscopy, and Masson trichrome staining in the diagnosis of alopecia, *J. Am. Acad. Dermatol.*, 2020, **82**(1), 247–249.

55 K. L. West, A. D. Proia and P. K. Puri, Fontana-Masson stain in fungal infections, *J. Am. Acad. Dermatol.*, 2017, **77**(6), 1119–1125.

56 J. Pan, W. Xiong, A. Zhang, H. Zhang, H. Lin, L. Gao, J. Ke, S. Huang, J. Zhang, J. Gu, A. C. Y. Chang and C. Wang, The imbalance of p53-park7 signaling axis induces iron homeostasis dysfunction in doxorubicin-challenged cardiomyocytes, *Adv. Sci.*, 2023, **10**(15), e2206007.

57 F. L. Wei, Y. Zhai, T. F. Wang, J. W. Zhao, C. L. Wang, Z. Tang, K. Shen, H. Wu, R. Zheng, M. R. Du, W. Heng, X. X. Li, X. D. Yan, Q. Y. Gao, Z. Guo, J. X. Qian and C. P. Zhou, Stem cell-homing biomimetic hydrogel promotes the repair of osteoporotic bone defects through osteogenic and angiogenic coupling, *Sci. Adv.*, 2024, **10**(44), eadq6700.